CMS Physics Analysis Summary

Contact: cms-pag-conveners-susy@cern.ch 2018/07/04

Search for supersymmetry using events with a photon, a lepton, and missing transverse momentum in pp collisions at $\sqrt{s} = 13$ TeV

The CMS Collaboration

Abstract

Results of a search for supersymmetry are presented using events with a photon, an electron or muon, and large missing transverse momentum. The analysis is based on a data sample corresponding to an integrated luminosity of 35.9 fb^{-1} of proton-proton collisions at $\sqrt{s} = 13$ TeV, produced by the CERN LHC and collected with the CMS detector in 2016. Models of supersymmetry with gauge-mediated supersymmetry breaking yield events with photons in the final state as well as electroweak gauge bosons decaying to leptons. Searches for events with both a photon and a lepton are sensitive probes of these models. No excess of events is observed beyond expectations from standard model processes. The results of the search are interpreted in the context of simplified models inspired by gauge-mediated supersymmetry breaking. These models are used to derive upper limits on the production cross sections of supersymmetric processes and set bounds on masses of supersymmetric particles.

1 Introduction

The search for supersymmetry (SUSY), a popular extension of the standard model (SM) of particle physics, is a central piece of the physics program at the CERN LHC. Models with general gauge-mediated (GGM) supersymmetry breaking [1–6] with the assumption that R-parity [7] is conserved often lead to final states containing photons and significant missing momentum [8–15]. Final states with an additional lepton offer the unique opportunity to probe the branching fractions of supersymmetric particles, making photon plus lepton signatures an important part of the SUSY search program at the LHC.

In GGM models, the lightest supersymmetric particle (LSP), taken to be the gravitino $\widetilde{\mathrm{G}}$, is both stable and weakly interacting. It escapes detection, leading to missing momentum in the event. Except for direct LSP pair production, each produced SUSY particle initiates a decay chain that yields the next-to-lightest supersymmetric particle (NLSP) decaying to the LPS, while the other final-state particles in the event depend sensitively on the nature of the NLSP. In most GGM models, the NLSP is taken to be a bino- or wino-like neutralino, where the bino and wino are the superpartners of the SM U(1) and SU(2) gauge fields, respectively. Typically, a neutralino $\widetilde{\chi}^0$ will decay to a photon or a Z boson, while a charged NLSP $\widetilde{\chi}^{\pm}$ will produce a W boson that can decay leptonically.

In this note, the results are presented of a search for SUSY in events with at least one photon γ, one lepton ℓ (electron or muon), and large missing transverse momentum $p_{\mathrm{T}}^{\mathrm{miss}}$. This signature suppresses many SM backgrounds, avoiding the need for additional requirements such as associated jet activity. The possibility to separate events with low jet activity increases sensitivity to some SUSY scenarios such as electroweak production of SUSY particles. The data sample corresponds to an integrated luminosity of $35.9\,\mathrm{fb}^{-1}$ of pp collision data at $\sqrt{s} = 13\,\mathrm{TeV}$, collected with the CMS detector at the CERN LHC in 2016. Similar searches were conducted by the ATLAS [16] and CMS [17, 18] experiments at $\sqrt{s} = 7$ and 8 TeV. None of these analyses observed any significant excess of events over their respective SM predictions. This note substantially improves on the sensitivity of the previous CMS result obtained at $\sqrt{s} = 8\,\mathrm{TeV}$ [19].

The Feynman diagrams in Fig. 1 provide examples of the decays studied in this analysis. Simplified models [20] are used for the interpretation of the results. These models assume gluino pair production (T5Wg), squark pair production (T6Wg), or the direct electroweak production of a neutralino and chargino (TChiWg). For simplicity, we assume the $\widetilde{\chi}^0$ and $\widetilde{\chi}^{\pm}$ are mass-degenerate co-NLSPs and are therefore produced at equal rates. The decay of the NLSP $\widetilde{\chi}^{\pm}$ ($\widetilde{\chi}^0$) produces a gravitino $\widetilde{\mathrm{G}}$ LSP with a W (γ). We assume a 50% branching fraction to either the $\widetilde{\chi}^0$ or the $\widetilde{\chi}^{\pm}$, and 100% branching fractions for the decays $\widetilde{\chi}^0 \to \gamma\widetilde{\mathrm{G}}$ and $\widetilde{\chi}^{\pm} \to \mathrm{W}^{\pm}\widetilde{\mathrm{G}}$.

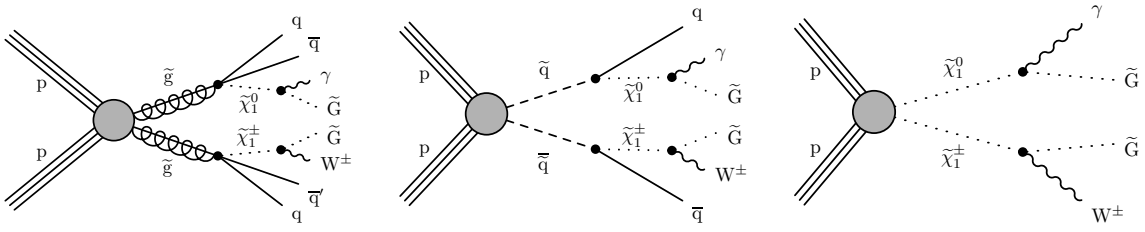

Figure 1: Feynman diagrams showing the production and decay modes of the signal models T5Wg (left), T6Wg (center), and TChiWg (right) considered in this analysis.

The note is organized as follows. In Section 2, we describe the CMS detector used to collect the data. The data samples and object definitions used in the analysis are described in Section 3,

and the details of the event selection are given in Section 4. The methods for estimating the backgrounds in the analysis are discussed in Section 5, the systematic uncertainties in Section 6 and the results are presented in Section 7. Section 8 summarizes our conclusions, including our exclusion limits in the simplified-model framework.

2 The CMS detector

The central feature of the CMS apparatus is a superconducting solenoid with an internal diameter of 6 m, providing an axial magnetic field of 3.8 T. Within the solenoid volume are several subdetector systems, each composed of a cylindrical barrel closed by two endcaps. At the core sits a silicon pixel and strip tracker, providing a precise measurement of the trajectories of charged particles. The energy of photons and electrons is measured by a lead tungstate crystal electromagnetic calorimeter (ECAL), covering the pseudorapidity range $|\eta| < 1.479$ in the barrel and $1.479 < |\eta| < 3.0$ in the endcap. Surrounding the ECAL is a brass and scintillator sampling hadron calorimeter with $|\eta| < 3.0$ coverage. Muons are measured in gas-ionization detectors embedded in the steel flux-return yoke outside the solenoid. Forward calorimeters extend the calorimeter coverage up to $|\eta| = 5.0$.

In the barrel section of the ECAL, an energy resolution of about 1% is achieved for unconverted and late-converting photons with transverse momentum $p_{\mathrm{T}} \approx 10\,\mathrm{GeV}$. The remaining barrel photons have a resolution of about 1.3% up to $|\eta| < 1.0$, rising to about 2.5% for $|\eta| = 1.4$ [21].

The electron momentum is determined by combining the energy measurement in the ECAL with the momentum measurement in the tracker. The momentum resolution for electrons with transverse momentum $p_{\mathrm{T}} \approx 45\,\mathrm{GeV}$ from $\mathrm{Z} \to \mathrm{e}^{+}\mathrm{e}^{-}$ decays ranges from 1.7% for non-showering electrons in the barrel region to 4.5% for showering electrons in the endcaps [22].

Muons are measured in the range $|\eta| < 2.4$, with detector elements based on three technologies: drift tubes, cathode strip chambers, and resistive plate chambers. Through the matching of track segments measured in the muon detectors with tracks measured in the tracker, a transverse momentum resolution of 1.3–2.0% is achieved for barrel muons with $20 < p_{\mathrm{T}} < 100\,\mathrm{GeV}$. In the endcaps, the resolution increases to a maximum of about 6%. The p_{T} resolution in the barrel is better than 10% for muons with transverse momentum up to 1 TeV [23].

A detailed description of the CMS detector, together with the definition of the coordinate system used and the relevant kinematic variables, can be found in Ref. [24].

3 Object reconstruction and simulated samples

Physics objects are defined using the particle-flow (PF) algorithm [25], which reconstructs and identifies individual particles through an optimized combination of information from different elements of the CMS detector. The PF candidates are classified as photons, charged hadrons, neutral hadrons, electrons, or muons. The PF method also allows the identification and mitigation of particles from additional proton-proton interactions from the same or nearby beam crossings (pileup).

Photons are reconstructed from clusters of energy deposits in the ECAL. To distinguish photon candidates from electrons, photon objects are rejected if a matching pixel track segment from the silicon tracker is identified. Photon candidates used in this analysis are identified with a set of loose quality criteria with an average selection efficiency of 90%. The photon identification criteria require the energy deposit in the HCAL tower behind the cluster to be less than 6% of

the ECAL energy, and the shower shape in the η direction to be consistent with the shower from a real photon. In addition, the photons are required to have more than 50% of the cluster energy deposited in the 3×3 crystals centered on the most energetic crystal. To further suppress the misidentification of hadrons as photons, a PF-based isolation requirement is imposed. The isolation variable is calculated by summing the magnitude of the momentum of all PF charged hadrons, neutral hadrons, and other photons within a cone of $\Delta R \equiv \sqrt{(\Delta\eta)^2 + (\Delta\phi)^2}$ around the candidate photon direction and required not to exceed fixed values defined to achieve a desirable balance between the identification efficiency and misidentification rate. The photon object that is being identified is not included in the isolation sums, and charged hadrons are included only if they are associated with the primary pp interaction vertex, which is defined as the vertex with the highest $\sum p_{\mathrm{T}}^2$ of associated tracks. The p_{T} sums are corrected for contributions from pileup.

Electrons are reconstructed by associating a track reconstructed in the silicon tracker to an ECAL cluster. The electron candidates are required to be within the fiducial region of $|\eta| < 2.5$, where the tracker coverage ends. Identification of electrons is based on the shower shape of the ECAL cluster, the HCAL to ECAL energy ratio, the geometrical matching between the cluster and the track, the quality of the track reconstruction, and the isolation variable. To enhance the identification efficiency, the isolation variable is calculated from the momenta of PF photons, charged hadrons, and neutral hadrons within a ΔR cone whose radius is variable depending on the electron p_{T}, and also corrected for the effects of pileup.

The reconstruction of muons is based on associating tracks from the silicon tracker to those in the muon system. A set of muon identification criteria, based on the goodness of track fit and quality of muon reconstruction, are applied to select the muon candidates targeting a greater than 98% efficiency for true muons [26]. Muons are also required to be isolated from other objects in the event using a similar isolation variable [26] as in the electron identification.

Jets are reconstructed using all PF candidates that are clustered using the anti-k_{T} algorithm [27, 28] with a distance parameter of 0.4. The jet energies are corrected for detector responses and offset energy from pileup [29]. Jet candidates considered in this analysis are required to have $p_{\mathrm{T}} > 30\,\mathrm{GeV}$, be within the $|\eta| < 2.5$ region, and be consistent with an origin at the primary vertex. The missing transverse momentum vector $\vec{p}_{\mathrm{T}}^{\,\mathrm{miss}}$ is given by the negative of the vector sum of the transverse momenta of all PF objects, with jet-energy corrections applied. The magnitude of $\vec{p}_{\mathrm{T}}^{\,\mathrm{miss}}$ is referred to as the missing transverse momentum $p_{\mathrm{T}}^{\mathrm{miss}}$. Since the CMS detector is nearly hermetic, accurate measurements of $p_{\mathrm{T}}^{\mathrm{miss}}$ are possible. Dedicated filters are applied to remove events with $p_{\mathrm{T}}^{\mathrm{miss}}$ induced by beam halo, noise in the detector, or poorly reconstructed muons.

Monte Carlo (MC) simulated events are used to model the SM backgrounds, validate the background estimation methods, and study the SUSY signal yields. Samples of the Wγ events are generated with MADGRAPH5_aMC@NLO 2.3.3 [30] at leading order (LO), while the Zγ, Drell–Yan, WW($+\gamma$), WZ($+\gamma$), and $\mathrm{t\bar{t}}$ ($+\gamma$) processes are generated at next-to-leading order (NLO). The generated events are propagated using PYTHIA 8.2 [31] with the CUETP8M1 generator tune [32] for simulation of parton showering and hadronization. The Zγ, Drell–Yan, WW($+\gamma$), WZ($+\gamma$), and $\mathrm{t\bar{t}}$ ($+\gamma$) samples are scaled to the integrated luminosity using the cross sections at NLO precision. For the Wγ sample, a next-to-NLO (NNLO) scale factor of 1.34 [33] is applied to the LO cross section to account for higher-order corrections. The CMS detector response is simulated using a GEANT4-based [34] package. Pileup with additional proton-proton interactions is modeled in the simulation by overlaying minimum-bias events on the corresponding hard-scattering events.

To improve the MADGRAPH modeling of initial-state radiation (ISR), which affects the total transverse momentum (p_T^{ISR}) of the event, the p_T^{ISR} distributions of the MC Wγ and Zγ events are weighted to agree with that of data. This reweighting procedure is based on studies of the transverse momentum of Z boson events [35]. The reweighting factors range from 1.11 at $p_T^{ISR} \approx 125\,\text{GeV}$ to 0.64 for $p_T^{ISR} > 300\,\text{GeV}$. We take the deviation of the reweighting factors from 1.0 as an estimate of the systematic uncertainty in the reweighting procedure.

4 Event selection

The analysis is performed in both the eγ and $\mu\gamma$ channels. The eγ data sample is collected using a diphoton trigger [36] requiring at least two isolated electromagnetic objects with a p_T threshold of 30 and 18 GeV for the highest-p_T (leading) and second-highest-p_T (subleading) electromagnetic object, respectively, that satisfy loose identification criteria and possess an invariant mass $M_{\gamma\gamma} > 90\,\text{GeV}$. The trigger does not veto photon objects that can be matched to a track, allowing events with a photon and an electron to also pass the trigger selections. The $\mu\gamma$ events are collected using a combination of two muon-photon triggers, one requiring the presence of an isolated photon with $p_T > 30\,\text{GeV}$ and a muon with $p_T > 17\,\text{GeV}$, and the other using symmetric p_T thresholds of 38 GeV for both objects, with no isolation criteria. With the selection criteria described below, the trigger efficiency for the investigated SUSY signal models is found to be fully efficient for both channels.

Candidate signal events are required to contain at least one isolated photon with $p_T > 35\,\text{GeV}$ and $|\eta| < 1.4442$ and at least one isolated electron (muon) with $p_T > 25\,\text{GeV}$ and $|\eta| < 2.5$ (2.4). To ensure a high reconstruction efficiency, electrons in the barrel-endcap transition region $1.44 < |\eta| < 1.56$ are rejected. To suppress events with photons from final-state radiation, photon candidates are vetoed if they are within $\Delta R < 0.3$ of any reconstructed electron or muon. In addition, the highest-p_T photon is required to be separated from the highest-p_T lepton by $\Delta R > 0.8$. In the eγ channel, the e-γ pair must have an invariant mass at least 10 GeV greater than the nominal Z boson mass [37] to reduce the contribution of $Z \to e^+e^-$ events, where one of the electrons is misidentified as a photon.

For each event we compute the transverse mass M_T of the lepton-p_T^{miss} system to help discriminate between the SUSY signal and SM backgrounds. The quantity M_T is defined as $M_T = \sqrt{(2p_T^{\ell} p_T^{miss}[1 - \cos(\Delta\phi(\ell, \vec{p}_T^{miss})]}$, where p_T^{ℓ} is the magnitude of the lepton transverse momentum and $\Delta\phi$ is the difference in azimuthal angle between the direction of the lepton and $\vec{p}_T^{miss}$. The signal region is defined as $p_T^{miss} > 120\,\text{GeV}$ and $M_T > 100\,\text{GeV}$. Models with strongly produced SUSY particles lead to final states with significant hadronic activity in the form of jets. To provide additional sensitivity to these models, we define the variable H_T as the scalar sum of the momenta of all jets that are separated from the candidate photon and lepton by $\Delta R > 0.4$. The signal region is later divided into search regions as a function of p_T^{miss}, photon p_T, and H_T.

5 Background estimation

The SM backgrounds of events with one lepton, one photon, and p_T^{miss} in the final state mainly arise from three sources. The first consists of events without a directly produced (prompt) photon. This includes events with a photon that does not originate from the original hard-scattering process but from a nearby vertex, as well as events with an object such as an electron or an electromagnetically rich jet that is misidentified as a photon. The second source of back-

ground events are those without a prompt lepton. These typically result from the misidentification of a jet as a lepton, or from a jet caused by the hadronization of a heavy-flavor quark, which produces a lepton via the semileptonic decay of the corresponding heavy-flavor meson or baryon. The final contribution to the background comes from electroweak processes, primarily Wγ and Zγ production. This category also includes rarer processes such as WWγ, WZγ, and $\mathrm{t\bar{t}}\,\gamma$, referred to as rare EWK processes.

The contribution from electroweak processes is estimated via simulation, while the backgrounds due to misidentified photons and misidentified leptons are estimated from the data as described below.

5.1 Backgrounds from misidentified photons

Photon candidates are considered "fake" if they are not produced directly in the hard-scattering process, or if they result from a misidentified object. The latter constitute the majority of misidentified photons and can occur if a large fraction of the energy of a jet is carried by a neutral pion that decays to two almost collinear photons, or an electron fails to register hits in the pixel tracker and is reconstructed as a photon. Events with photons from jets can arise from the process $\mathrm{W}(\to \ell\nu)+$ jets, where a π^0 or η^0 in the jet decays to photons. Events with misidentified photons from electrons can arise from Drell–Yan dielectron production ($\mathrm{q\bar{q}} \to \gamma^* \to \mathrm{e^+e^-}$), as well as $\mathrm{t\bar{t}}$ events with an electron in the final state.

The misidentified-photon background is estimated from collision data by determining the rate of misidentification and applying it to events from a control sample. First, the control or proxy sample is formed by replacing the photon candidate with a photon-like object, which can be achieved by inverting some of the photon identification criteria, while keeping the other selection requirements identical to those for signal candidates. Second, the misidentification rate or transfer factor is then defined as the ratio of the number of misidentified photons to the total number of photon-like objects in the control sample. The transfer factor is derived in a control region, such as $p_{\mathrm{T}}^{\mathrm{miss}} < 70\,\mathrm{GeV}$, and then extrapolated to the signal region.

Electron-proxy samples are constructed by requiring the candidate photon to either have a seed in the pixel detector or to geometrically match a reconstructed electron within $\Delta R < 0.03$. The misidentification rate is estimated using the tag-and-probe method [38] on a sample of $\mathrm{Z} \to \mathrm{e^+e^-}$ events in data. The rate is derived in bins of three variables, the p_{T} and $|\eta|$ of the probe objects, and the number of vertices in the event N_{vtx}. Parameterized functions are used to model the dependence of the misidentification rate on p_{T} and N_{vtx}, and binned values are used for the $|\eta|$ dependence. The measured misidentification rate varies from 2.3% for $p_{\mathrm{T}} = 35\,\mathrm{GeV}$ to 1.2% for $p_{\mathrm{T}} > 180\,\mathrm{GeV}$. Transfer factors are assigned on an event-by-event basis to the proxy samples. The verify the correctness of this background estimation method, it is tested on simulated Drell–Yan and $\mathrm{t\bar{t}}$ events. As shown in Fig. 2, good agreement is achieved between the e-to-γ misidentification estimation method and the true background as obtained from the MC truth information of the simulated data.

To estimate the jet-to-photon misidentification background, a hadronic-proxy sample is constructed by inverting one of the variables characterizing the ECAL cluster shape ($\sigma_{\eta\eta}$ in Ref. [22]) and isolation criteria. The transfer factor for the hadronic-proxy sample is determined through an assessment of the fraction of events with jet-to-photon misidentification among the photon candidates. This fraction is denoted as the "hadron fraction". The measurement is performed in the region $p_{\mathrm{T}}^{\mathrm{miss}} < 70\,\mathrm{GeV}$ from a fit to the $\sigma_{\eta\eta}$ distribution based on two templates, one representing pure photons obtained from $\gamma+$jet simulated MC events and one modeling the events with jet-to-photon misidentification, where the template for those events is obtained by

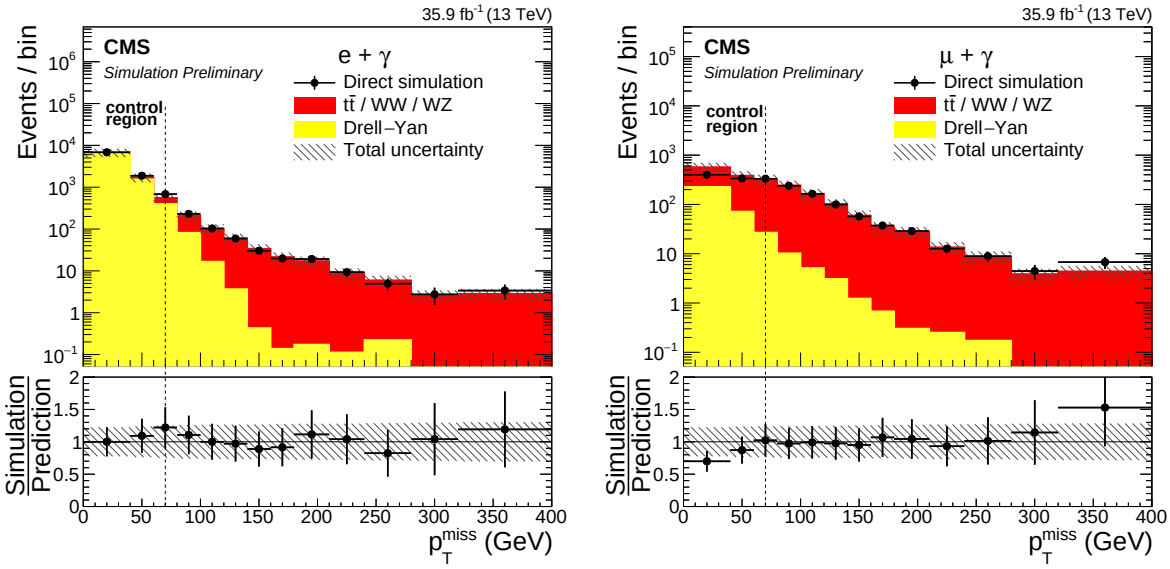

Figure 2: Verification of the e-to-γ misidentification estimation method using simulated data. The predicted $p_{\mathrm{T}}^{\mathrm{miss}}$ distribution for events with misidentified photons in the eγ(left) and $\mu\gamma$ (right) channel from direct simulation (points) and from using the proxy sample estimation method from data (histograms). The vertical bars on the points show the statistical uncertainty in the simulation, while the horizontal bars give the bin widths. The lower panels show the ratio of the predictions from direct simulation to those from the proxy sample method. The vertical bars on the points show again the statistical uncertainty, and the hatched areas give the quadrature sum of the statistical and systematic uncertainties in the simulated background.

inverting the isolation requirement on the signal-photon candidates. The fit to the $\sigma_{\eta\eta}$ distribution is performed in ranges of photon p_{T}. The resulting hadron fraction varies from 0.47 to 0.04 for the eγ channel, and 0.18 to 0.04 for the $\mu\gamma$ channel. The p_{T} distribution of the jet-to-photon backgrounds in the control region is obtained by multiplying the p_{T} distribution of the photon candidates by the hadron fraction. To extrapolate the result to high-p_{T} photons, the p_{T} shape of the jet-to-photon backgrounds and the proxy samples are modeled with parameterized functions, and the ratio between these two functions is used to assign event-by-event transfer factors in the signal region.

5.2 Electroweak and misidentified-lepton backgrounds

The SM backgrounds in final states with a lepton, a photon, and $p_{\mathrm{T}}^{\mathrm{miss}}$ are dominated by the production of massive vector bosons (W, Z) in association with a photon, denoted $V\gamma$ production. In particular, neutrinos from the W boson leptonic decay escape the detector, producing significant $p_{\mathrm{T}}^{\mathrm{miss}}$. The shape of the $p_{\mathrm{T}}^{\mathrm{miss}}$ distribution from the $V\gamma$ background is modeled by simulation, and the normalization factors are determined together with those of the misidentified-lepton backgrounds. A lepton is considered to be misidentified if it doesn't originate from a prompt W or Z boson decay. This includes leptons from heavy-flavor and light-meson decays, misidentified jets, and electrons from photon conversions. Similar to the misidentified-photon background, the shape of the misidentified-lepton backgrounds are modeled by proxy samples, which are formed by inverting the isolation requirement of the lepton while keeping other requirements unchanged. For electrons, the cluster shape and the quality of the cluster-to-track matching are also inverted to include more hadronic objects.

The normalization of the $V\gamma$ and misidentified lepton backgrounds is determined by a two-component signal plus background template fit to the distribution of $\Delta\phi(\ell, p_{\mathrm{T}}^{\mathrm{miss}})$, the azimuthal

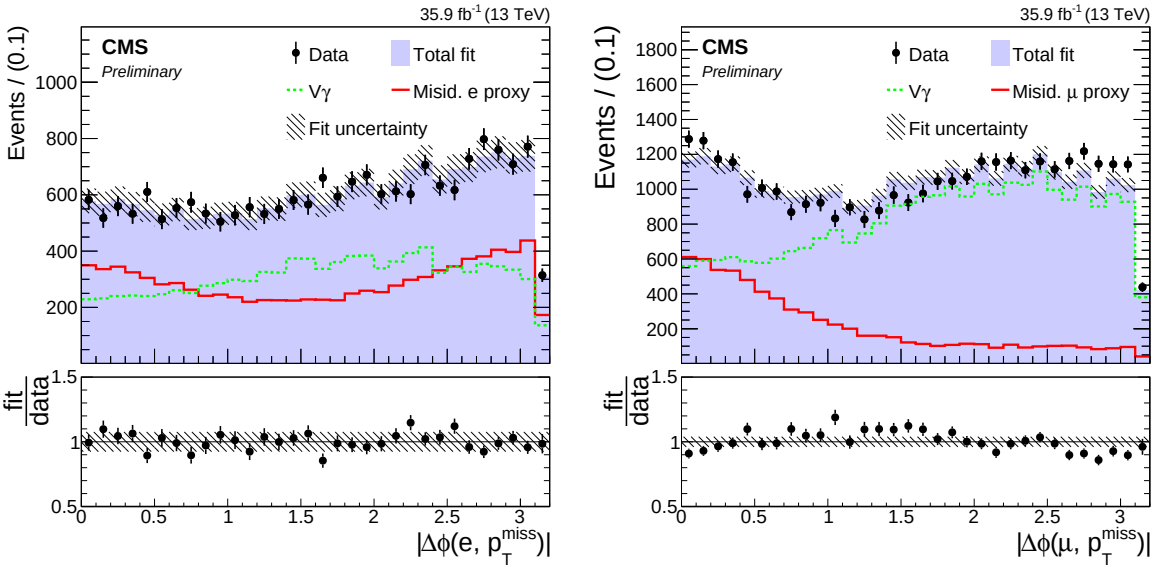

Figure 3: The post-fit $\Delta\phi(\ell, p_{\mathrm{T}}^{\mathrm{miss}})$ distributions for the $V\gamma$ (dashed-green) and misidentified-lepton (solid-red) backgrounds. The black points show the data in the $40 < p_{\mathrm{T}}^{\mathrm{miss}} < 70\,\mathrm{GeV}$ control region with the fit result overlaid for the eγ (left) and $\mu\gamma$ (right) channels, while the grey-blue distribution gives the fit result and the hatched area indicates the fit uncertainty. The vertical bars on the points represent the statistical uncertainty. The lower panels show the ratio of the fit result to the data. The vertical bars on the points show the statistical uncertainty in the data, and the hatched areas give the fit uncertainty.

angular difference between the direction of the lepton and $\vec{p}_{\mathrm{T}}^{\mathrm{miss}}$ in the transverse plane. This fit is performed in the region $40 < p_{\mathrm{T}}^{\mathrm{miss}} < 70\,\mathrm{GeV}$, where the lower bound of 40 GeV is applied to reduce the contribution of $Z\gamma$ events. Expected contributions from the misidentified-photon and rare electroweak backgrounds such as WW($+\gamma$), WZ($+\gamma$), and $\mathrm{t\bar{t}}$ ($+\gamma$) processes are subtracted before the fit. The post-fit distribution of $\Delta\phi(\ell, p_{\mathrm{T}}^{\mathrm{miss}})$ is shown in Fig. 3 with the fit results overlaid. The resulting scale factors for the $e + \gamma$ channel are $SF_{V\gamma} = 1.17 \pm 0.23$ and $SF_{e-proxy} = 0.24 \pm 0.05$, while the scale factors for the $\mu + \gamma$ channel are $SF_{V\gamma} = 1.33 \pm 0.27$ and $SF_{\mu-proxy} = 0.62 \pm 0.12$, where the uncertainties are statistical only.

6 Systematic uncertainties

Table 1 summarizes the relative systematic uncertainties in the background estimation and signal expectation. The main sources of systematic uncertainties are the scale factors derived from the $\Delta\phi(\ell, p_{\mathrm{T}}^{\mathrm{miss}})$ template fit to the $V\gamma$ and misidentified-lepton backgrounds, and the cross sections used to normalize the rare EWK simulated samples. For the $V\gamma$ normalization, systematic uncertainties are obtained by varying the shape of the templates, the number of events that are subtracted from the fit target, and the renormalization and factorization scales of the simulations. For the rare EWK backgrounds, a 50% uncertainty is assigned to the cross sections to cover the difference between the calculated cross sections and the latest CMS measurements [39, 40].

The subdominant systematic uncertainties come from the modeling of the misidentified photons. Different choices of sidebands and parameterized functions are studied to evaluate the size of these systematic effects. The uncertainties in the number of misidentified photons with $p_{\mathrm{T}} < 200\,\mathrm{GeV}$ are less than 20%. A larger uncertainty above 20% only applies to the high-p_{T} bins, where the misidentified photons contribute less than 10% of the total background, re-

sulting in a small influence on the total background prediction. For the backgrounds that are obtained from simulation, systematic uncertainties from the jet energy scale (JES) and jet energy resolution (JER) are evaluated by varying the scale by one standard deviation around its nominal value. Finally, the uncertainty in the integrated luminosity of the CMS data sample is 2.6%.

Table 1: Summary of the systematic uncertainties affecting the SUSY signals and SM background estimates given in percent.

Source of uncertainty	SUSY signal	$e \to \gamma$ fakes	jet$\to \gamma$ fakes	jet$\to \ell$ fakes	$V + \gamma$	rare EWK
Jet energy scale	$0-10$	–	–	–	$0-15.6$	$0-22.5$
Jet energy resolution	$0-10$	–	–	–	$0-13.6$	$0-23$
ID and trigger efficiency	4	–	–	–	$1.4-6.5$	$1.3-6.5$
Cross section	$4.3-36.8$	–	–	–	–	50
e-faking-photon shape	–	$8.0-50.5$	–	–	–	–
Jet-faking-photon shape	–	–	$8.1-56.1$	–	–	–
Fake-lepton shape	–	–	–	$0-42.4$	–	–
ISR corrections	–	–	–	–	$2.6-57.8$	–
Normalization scale	–	–	–	20	20	–
Pileup uncertainty	$2-10$	–	–	–	–	–
Integrated luminosity	2.6	–	–	–	–	2.6

7 Results

Figure 4 shows the $p_{\mathrm{T}}^{\mathrm{miss}}$, p_{T}^{γ}, and H_{T} distributions of the observed data and predicted background, together with the systematic uncertainties in the background prediction. The $p_{\mathrm{T}}^{\mathrm{miss}}$ distribution includes all events with $M_{\mathrm{T}} > 100\,\mathrm{GeV}$, while the p_{T}^{γ} and H_{T} distributions only include events in the signal region. Two signal distributions, one from the TChiWg simplified model with NLSP mass of 800 GeV and the other from the T5Wg model with $M_{\tilde{\mathrm{g}}} = 1700\,\mathrm{GeV}$ and NLSP mass of 1000 GeV, are also overlaid. The data are compatible with the estimated SM backgrounds within the uncertainties.

To improve the sensitivity to different SUSY scenarios, the signal region for each lepton channel is further divided into 18 search regions: three bins of $p_{\mathrm{T}}^{\mathrm{miss}}$ ($120 < p_{\mathrm{T}}^{\mathrm{miss}} < 200\,\mathrm{GeV}$, $200 < p_{\mathrm{T}}^{\mathrm{miss}} < 400\,\mathrm{GeV}$, and $p_{\mathrm{T}}^{\mathrm{miss}} > 400\,\mathrm{GeV}$) in each of three H_{T} ranges ($0 < H_{\mathrm{T}} < 100\,\mathrm{GeV}$, $100 < H_{\mathrm{T}} < 400\,\mathrm{GeV}$, and $H_{\mathrm{T}} > 400\,\mathrm{GeV}$), plus two distinct ranges of photon p_{T} ($35 < p_{\mathrm{T}}^{\gamma} < 200\,\mathrm{GeV}$ and $p_{\mathrm{T}}^{\gamma} > 200\,\mathrm{GeV}$). Figure 5 shows a compilation of event yields from data and estimated backgrounds for each signal region as a function of the search bins. The observed data are consistent with the background prediction. The 10th and last bin in the eγ channel shows excesses above prediction with local significances of 2.3 and 1.2 standard deviations, respectively. In the corresponding regions of the $\mu\gamma$ channel, the data are compatible with the SM background prediction. Thus, we conclude that no significant excess of events beyond the SM expectation is observed.

8 Interpretation

The results are interpreted in the context of upper limits on the cross sections of the three simplified models introduced in Section 1. For each parameter point of the three models, a large number of hard-scattering simulation events are generated. These events are processed with a fast simulation of the CMS detector response [41]. A number of minimum-bias interactions are superimposed on the hard-scattering process in order to reproduce the pileup profile observed in data. The event selection applied to the simulated signal events is identical to that applied to

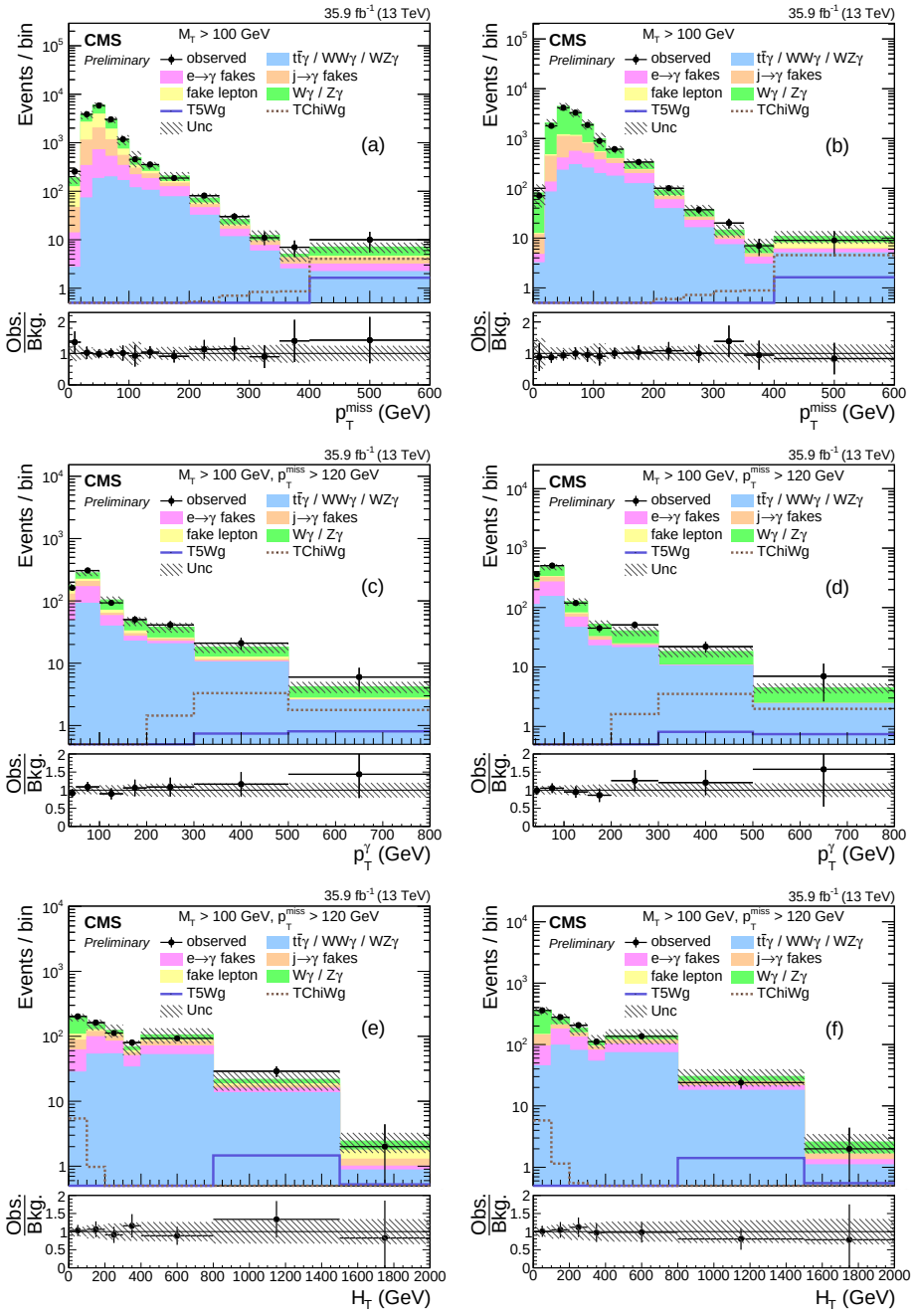

Figure 4: Distributions of $p_{\mathrm{T}}^{\mathrm{miss}}$ (a, b), p_{T}^{γ} (c, d), and H_{T} (e, f) from data (points) and simulated SM predictions (stacked histograms) for the eγ (left) and $\mu\gamma$ (right) channels. Simulated signal distributions from from the TChiWg model (dotted) with $M_{\tilde{\chi}^0/\tilde{\chi}^{\pm}} = 800\,\mathrm{GeV}$ and the T5Wg model (solid) with $M_{\tilde{\mathrm{g}}} = 1700\,\mathrm{GeV}$ are overlaid. The $p_{\mathrm{T}}^{\mathrm{miss}}$ distribution includes all events with $M_{\mathrm{T}} > 100\,\mathrm{GeV}$, while the p_{T}^{γ} and H_{T} distributions only include events with $M_{\mathrm{T}} > 100\,\mathrm{GeV}$ and $p_{\mathrm{T}}^{\mathrm{miss}} > 120\,\mathrm{GeV}$. The vertical bars on the points give the statistical uncertainty in the data. The horizontal bars show the bin widths. The lower panels display the ratio of the data to the total background prediction. The vertical bars on the points show the statistical uncertainty in the data, and the hatched areas give the quadrature sum of the statistical and systematic uncertainties in the simulated background.

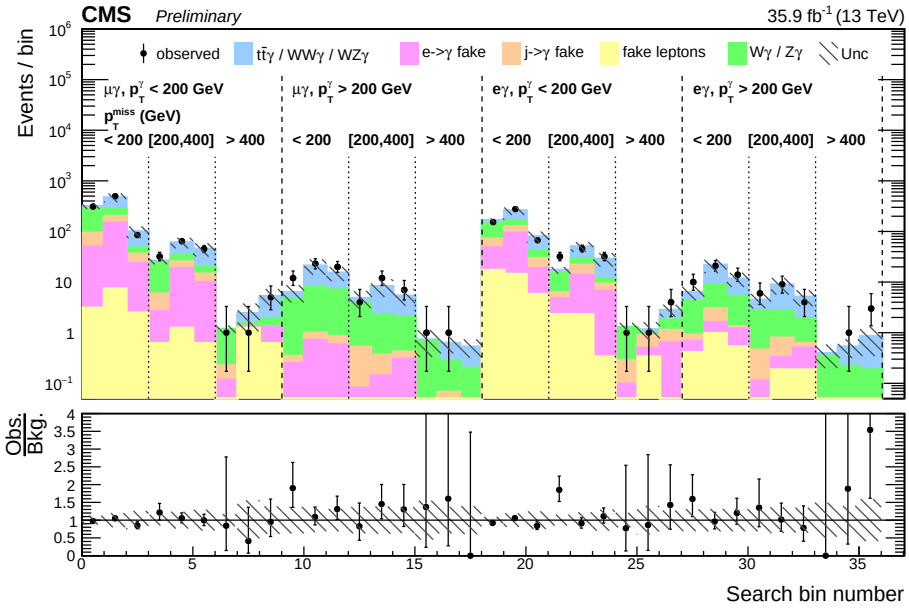

Figure 5: The number of signal events from data (points) and from simulated background (stacked histograms) for the 18 search bins in $p_{\mathrm{T}}^{\mathrm{miss}}$, H_{T}, and p_{T}^{γ} in the $\mu + \gamma$ channel (left) and the $e + \gamma$ channel (right). For each $p_{\mathrm{T}}^{\mathrm{miss}}$ range, the first, second, and last bins correspond to the H_{T} ranges [0,100], [100,400] and $>$ 400 GeV, respectively. The lower panel displays the ratio of the data to the background predictions. The vertical bars on the points show the statistical uncertainty in the data, and the hatched areas give the quadrature sum of the statistical and systematic uncertainties in the simulated background.

data, including the trigger requirements. The resulting event yields are weighted by correction factors to account for selection efficiency differences between data and simulation.

For each mass point of the signal models, a 95% confidence level (CL) upper limit on the signal production cross section is obtained calculating $\mathrm{CL_s}$ limits using the profiled likelihood as a test statistic and asymptotic formulas [42, 43]. The SM background prediction, signal expectation, and observed number of events in each signal-region bin of the eγ and $\mu\gamma$ channels are combined into one statistical interpretation, and studied as a multichannel counting experiment.

Figure 6 shows the observed limits for the TChiWg model as a function of NLSP masses, together with the theoretical cross sections for $\widetilde{\chi}^{\pm}\widetilde{\chi}^{0}$ pair production. The TChiWg model is initiated by the direct production of hypothetical particles $\widetilde{\chi}^{\pm}$ and $\widetilde{\chi}^{0}$, whose decays are restricted to $\mathrm{W}^{\pm}\widetilde{\mathrm{G}}$ and $\gamma\widetilde{\mathrm{G}}$, respectively. The gravitino $\widetilde{\mathrm{G}}$ is modeled as nearly massless. Assuming a 100% branching fraction for $\widetilde{\chi}^{0} \to \gamma\widetilde{\mathrm{G}}$, this search excludes NLSP masses up to 900 GeV.

In Figure 7, we present the cross section upper limits and mass exclusion contours for the T5Wg and T6Wg simplified models. The production cross section of the T5Wg (T6Wg) model is determined solely by $M_{\widetilde{\mathrm{g}}}$ ($M_{\widetilde{\mathrm{q}}}$). Nevertheless, the $M_{\widetilde{\mathrm{g}}/\widetilde{\mathrm{q}}} - M_{\widetilde{\chi}}$ mass difference affects the H_{T} and $p_{\mathrm{T}}^{\mathrm{miss}}$ spectra, resulting in nontrivial exclusion-limit contours in the $M_{\widetilde{\chi}}$-$M_{\widetilde{\mathrm{g}}/\widetilde{\mathrm{q}}}$ mass plane. The branching fraction for $\widetilde{g}(\widetilde{q}) \to \widetilde{\chi}^{0}/\widetilde{\chi}^{\pm}q\bar{q}$ is assumed to be 50%. For large $\widetilde{\chi}^{0}/\widetilde{\chi}^{\pm}$ masses, gluino (squark) masses are excluded up to 1700 (1400) GeV in the T5Wg (T6Wg) scenarios.

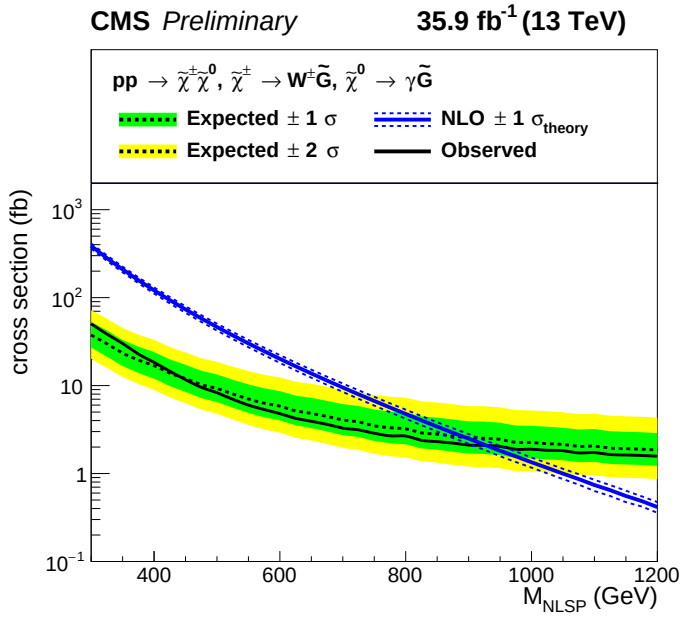

Figure 6: The observed and expected 95% CL upper limits on the production cross sections for the TChiWg simplified model, together with the theoretical cross sections. The inner (darker) band and outer (lighter) band around the expected upper limits indicate the regions containing 68 and 95%, respectively, of the distribution of limits expected under the background-only hypothesis. The band around the theoretical cross section gives the ± 1 standard deviation uncertainty in the cross section.

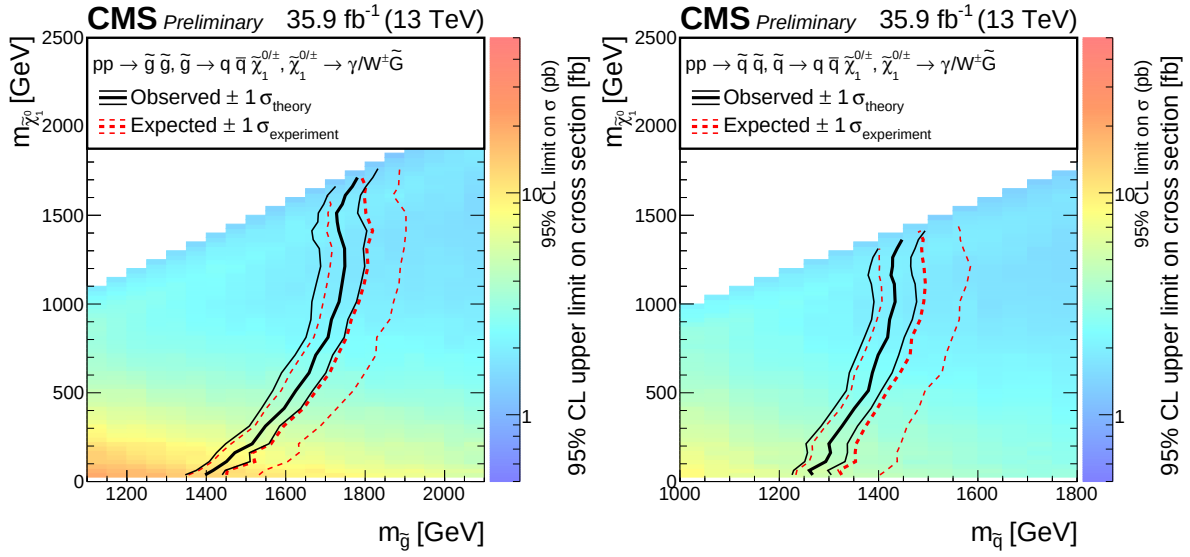

(a) (b)

Figure 7: The observed and expected 95% CL exclusion contours for $M_{\tilde{g}/\tilde{q}}$ versus $M_{\tilde{\chi}}$ (regions to the left of the curves are excluded) and the 95% CL upper limits on the pair production cross sections for the (a) T5Wg and (b) T6Wg simplified models. The upper limits on the cross section assume a 50% branching fraction for $\tilde{g}(\tilde{q}) \to \tilde{\chi}^0/\tilde{\chi}^{\pm} q\bar{q}$. The bands around the observed and expected exclusion contours indicate the ± 1 standard deviation range when including the experimental and theoretical uncertainties, respectively.

9 Summary

A search for supersymmetry with general gauge mediation in events with a photon, an electron or muon, and large missing transverse momentum is presented. This analysis is based on a sample of proton-proton collisions at $\sqrt{s} = 13$ TeV corresponding to an integrated luminosity of 35.9 fb^{-1} recorded by the CMS experiment in 2016. The data are examined in bins of the photon transverse energy, the magnitude of the missing transverse momentum, and H_T, the scalar sum of jet energies. The standard model background is evaluated primarily using control samples in the data, with simulation used to evaluate backgrounds from electroweak processes. The data is found to agree with the standard model expectation, without significant excess in the search region. The results of the search are interpreted as a 95% confidence level upper limits on the production cross section of supersymmetry particles in the context of simplified models motivated by gauge-mediated supersymmetry breaking. The TChiWg simplified model, based on direct electroweak production of a neutralino and chargino, is excluded for next-to-lightest supersymmetric particle masses below 900 GeV. For strong production models, such as the T5Wg simplified model of gluino pair production and the T6Wg model of squark pair production, this search excludes gluinos (squarks) with masses of up to 1700 (1400) GeV in the T5Wg (T6Wg) scenarios.

References

[1] M. Dine and W. Fischler, "A phenomenological model of particle physics based on supersymmetry", *Phys. Lett. B* **110** (1982) 227, doi:10.1016/0370-2693(82)91241-2.

[2] L. Alvarez-Gaume, M. Claudson, and M. B. Wise, "Low-energy supersymmetry", *Nucl. Phys. B* **207** (1982) 96, doi:10.1016/0550-3213(82)90138-9.

[3] C. R. Nappi and B. A. Ovrut, "Supersymmetric extension of the SU(3)xSU(2)xU(1) model", *Phys. Lett. B* **113** (1982) 175, doi:10.1016/0370-2693(82)90418-X.

[4] M. Dine and A. E. Nelson, "Dynamical supersymmetry breaking at low-energies", *Phys. Rev. D* **48** (1993) 1277, doi:10.1103/PhysRevD.48.1277, arXiv:hep-ph/9303230.

[5] M. Dine, A. E. Nelson, and Y. Shirman, "Low energy dynamical supersymmetry breaking simplified", *Phys. Rev. D* **51** (1995) 1362, doi:10.1103/PhysRevD.51.1362, arXiv:hep-ph/9408384.

[6] M. Dine, A. E. Nelson, Y. Nir, and Y. Shirman, "New tools for low-energy dynamical supersymmetry breaking", *Phys. Rev. D* **53** (1996) 2658, doi:10.1103/PhysRevD.53.2658, arXiv:hep-ph/9507378.

[7] G. R. Farrar and P. Fayet, "Phenomenology of the production, decay, and detection of new hadronic states associated with supersymmetry", *Phys. Lett. B* **76** (1978) 575, doi:10.1016/0370-2693(78)90858-4.

[8] S. Dimopoulos, G. F. Giudice, and A. Pomarol, "Dark matter in theories of gauge mediated supersymmetry breaking", *Phys. Lett. B* **389** (1996) 37, doi:10.1016/S0370-2693(96)01241-5, arXiv:hep-ph/9607225.

[9] S. P. Martin, "Generalized messengers of supersymmetry breaking and the sparticle mass spectrum", *Phys. Rev. D* **55** (1997) 3177, doi:10.1103/PhysRevD.55.3177, arXiv:hep-ph/9608224.

[10] E. Poppitz and S. P. Trivedi, "Some remarks on gauge mediated supersymmetry breaking", *Phys. Lett. B* **401** (1997) 38, doi:10.1016/S0370-2693(97)00367-5, arXiv:hep-ph/9703246.

[11] P. Meade, N. Seiberg, and D. Shih, "General gauge mediation", *Prog. Theor. Phys. Suppl.* **177** (2009) 143, doi:10.1143/PTPS.177.143, arXiv:0801.3278.

[12] M. Buican, P. Meade, N. Seiberg, and D. Shih, "Exploring general gauge mediation", *JHEP* **03** (2009) 016, doi:10.1088/1126-6708/2009/03/016, arXiv:0812.3668.

[13] S. Abel, M. J. Dolan, J. Jaeckel, and V. V. Khoze, "Phenomenology of pure general gauge mediation", *JHEP* **12** (2009) 001, doi:10.1088/1126-6708/2009/12/001, arXiv:0910.2674.

[14] L. M. Carpenter, M. Dine, G. Festuccia, and J. D. Mason, "Implementing general gauge mediation", *Phys. Rev. D* **79** (2009) 035002, doi:10.1103/PhysRevD.79.035002, arXiv:0805.2944.

[15] T. T. Dumitrescu, Z. Komargodski, N. Seiberg, and D. Shih, "General messenger gauge mediation", *JHEP* **05** (2010) 096, doi:10.1007/JHEP05(2010)096, arXiv:1003.2661.

[16] ATLAS Collaboration, "Search for photonic signatures of gauge-mediated supersymmetry in 8 TeV pp collisions with the ATLAS detector", *Phys. Rev. D* **92** (2015) 072001, doi:10.1103/PhysRevD.92.072001, arXiv:1507.05493.

[17] CMS Collaboration, "Search for supersymmetry in events with a lepton, a photon, and large missing transverse energy in pp collisions at $\sqrt{s} = 7$ TeV", *JHEP* **06** (2011) 093, doi:10.1007/JHEP06(2011)093, arXiv:1105.3152.

[18] CMS Collaboration, "Search for supersymmetry with photons in pp collisions at $\sqrt{s} = 8$ TeV", *Phys. Rev. D* **92** (2015) 072006, doi:10.1103/PhysRevD.92.072006, arXiv:1507.02898.

[19] CMS Collaboration, "Search for supersymmetry in events with a photon, a lepton, and missing transverse momentum in pp collisions at $\sqrt{s} = 8$ TeV", *Phys. Lett. B* **757** (2016) 6, doi:10.1016/j.physletb.2016.03.039, arXiv:1508.01218.

[20] CMS Collaboration, "Interpretation of searches for supersymmetry with simplified models", *Phys. Rev. D* **88** (2013) 052017, doi:10.1103/PhysRevD.88.052017, arXiv:1301.2175.

[21] CMS Collaboration, "Performance of photon reconstruction and identification with the CMS detector in proton-proton collisions at $\sqrt{s} = 8$ TeV", *JINST* **10** (2015) P08010, doi:10.1088/1748-0221/10/08/P08010, arXiv:1502.02702.

[22] CMS Collaboration, "Performance of electron reconstruction and selection with the CMS detector in proton-proton collisions at $\sqrt{s} = 8$ TeV", *JINST* **10** (2015) P06005, doi:10.1088/1748-0221/10/06/P06005, arXiv:1502.02701.

[23] CMS Collaboration, "Performance of CMS muon reconstruction in pp collision events at $\sqrt{s} = 7$ TeV", *JINST* **7** (2012) P10002, doi:10.1088/1748-0221/7/10/P10002, arXiv:1206.4071.

[24] CMS Collaboration, "The CMS experiment at the CERN LHC", *JINST* **3** (2008) S08004, doi:10.1088/1748-0221/3/08/S08004.

[25] CMS Collaboration, "Particle-flow reconstruction and global event description with the CMS detector", *JINST* **12** (2017) P10003, doi:10.1088/1748-0221/12/10/P10003, arXiv:1706.04965.

[26] CMS Collaboration, "Performance of the CMS muon detector and muon reconstruction with proton-proton collisions at $\sqrt{s} = 13$ TeV", arXiv:1804.04528.

[27] M. Cacciari, G. P. Salam, and G. Soyez, "The anti-k_t jet clustering algorithm", *JHEP* **04** (2008) 063, doi:10.1088/1126-6708/2008/04/063, arXiv:0802.1189.

[28] M. Cacciari, G. P. Salam, and G. Soyez, "FastJet user manual", *Eur. Phys. J. C* **72** (2012) 1896, doi:10.1140/epjc/s10052-012-1896-2, arXiv:1111.6097.

[29] M. Cacciari and G. P. Salam, "Pileup subtraction using jet areas", *Phys. Lett. B* **659** (2008) 119, doi:10.1016/j.physletb.2007.09.077, arXiv:0707.1378.

[30] J. Alwall et al., "The automated computation of tree-level and next-to-leading order differential cross sections, and their matching to parton shower simulations", *JHEP* **07** (2014) 079, doi:10.1007/JHEP07(2014)079, arXiv:1405.0301.

[31] T. Sjostrand et al., "An introduction to PYTHIA 8.2", *Comput. Phys. Commun.* **191** (2015) 159, doi:10.1016/j.cpc.2015.01.024, arXiv:1410.3012.

[32] CMS Collaboration, "Event generator tunes obtained from underlying event and multiparton scattering measurements", *Eur. Phys. J. C* **76** (2016) 155, doi:10.1140/epjc/s10052-016-3988-x, arXiv:1512.00815.

[33] G. Bozzi et al., "Production of Drell–Yan lepton pairs in hadron collisions: Transverse-momentum resummation at next-to-next-to-leading logarithmic accuracy", *Phys. Lett. B* **696** (2011) 207, doi:10.1016/j.physletb.2010.12.024, arXiv:1007.2351.

[34] GEANT4 Collaboration, "GEANT4—a simulation toolkit", *Nucl. Instrum. Meth. A* **506** (2003) 250, doi:10.1016/S0168-9002(03)01368-8.

[35] CMS Collaboration, "Search for top-squark pair production in the single-lepton final state in pp collisions at $\sqrt{s} = 8$ TeV", *Eur. Phys. J. C* **73** (2013) 2677, doi:10.1140/epjc/s10052-013-2677-2, arXiv:1308.1586.

[36] CMS Collaboration, "The CMS trigger system", *JINST* **12** (2017) P01020, doi:10.1088/1748-0221/12/01/P01020, arXiv:1609.02366.

[37] Particle Data Group, C. Patrignani et al., "Review of particle physics", *Chin. Phys. C* **40** (2016) 100001, doi:10.1088/1674-1137/40/10/100001.

[38] CMS Collaboration, "Measurement of the inclusive W and Z production cross sections in pp collisions at $\sqrt{s} = 7$ TeV", *JHEP* **10** (2011) 132, doi:10.1007/JHEP10(2011)132, arXiv:1107.4789.

[39] CMS Collaboration, "Measurement of the semileptonic $\mathrm{t\bar{t}}+\gamma$ production cross section in pp collisions at $\sqrt{s} = 8$ TeV", *JHEP* **10** (2017) 006, doi:10.1007/JHEP10(2017)006, arXiv:1706.08128.

[40] CMS Collaboration, "Measurement of the $t\bar{t}$ production cross section using events in the eμ final state in pp collisions at $\sqrt{s} = 13\,\text{TeV}$", *Eur. Phys. J. C* **77** (2017) 172, doi:10.1140/epjc/s10052-017-4718-8, arXiv:1611.04040.

[41] CMS Collaboration, "The fast simulation of the CMS detector at LHC", *J. Phys. Conf. Ser.* **331** (2011) 032049, doi:10.1088/1742-6596/331/3/032049.

[42] T. Junk, "Confidence level computation for combining searches with small statistics", *Nucl. Instrum. Meth. A* **434** (1999) 435, doi:10.1016/S0168-9002(99)00498-2, arXiv:hep-ex/9902006.

[43] A. L. Read, "Presentation of search results: The CL_s technique", *J. Phys. G* **28** (2002) 2693, doi:10.1088/0954-3899/28/10/313.